Revisiting the Saffman-Taylor Experiment: Imbibition Patterns and Liquid-Entrainment Transitions

Bertrand Levaché[1,2] and Denis Bartolo[1,3]
[1]PMMH-CNRS–ESPCI ParisTech-Université Paris 6-Université Paris 7, 10, rue Vauquelin, 75005 Paris, France
[2]Total France, Pole d'Etudes et de Recherche de Lacq, BP47-64170 Lacq, France
[3]Ecole Normale Supérieure de Lyon, CNRS, Université de Lyon, 46, allée d'Italie, 69007 Lyon, France
(Received 5 February 2014; revised manuscript received 14 May 2014; published 23 July 2014)

We revisit the Saffman-Taylor experiment focusing on the forced-imbibition regime where the displacing fluid wets the confining walls. We demonstrate a new class of invasion patterns that do not display the canonical fingering shapes. We evidence that these unanticipated patterns stem from the entrainment of thin liquid films from the moving meniscus. We then theoretically explain how the interplay between the fluid flow at the contact line and the interface deformations results in the destabilization of liquid interfaces. In addition, this minimal model conveys a unified framework which consistently accounts for all the liquid-entrainment scenarios that have been hitherto reported.

DOI: 10.1103/PhysRevLett.113.044501 PACS numbers: 47.20.Ma, 47.54.-r, 68.08.Bc

What liquid should be used to clean a hydrophilic container filled with an organic fluid? As it turns out, this seemingly trivial question is of major importance in a number of industrial process, including enhanced recovery of the so-called heavy oils. An elementary thermodynamic reasoning would suggest using an aqueous liquid making the smallest possible contact angle with the container walls. In this Letter we show that the answer is actually more subtle when the dynamics of the fluid interfaces is considered.

From a fundamental perspective, liquid-liquid interfaces driven past solid substrates have been extensively used as a proxy to investigate nonlinear-pattern formation such as Laplacian growth processes [1–4]. Until now, the overwhelming majority of the experiments have been performed in the drainage regime, where a low-viscosity fluid displaces a high-viscosity fluid which preferentially wets the solid. From the Saffman-Taylor fingers growing in Hele-Shaw cells [1,2,5] to the fractal patterns found in porous media [3,4,6], the salient features of all the drainage patterns are very well captured by coarse-grained front-propagation models that all discard the details of the interactions between the liquid and the solid walls. On the other hand, the experiments on imbibition dynamics, where the less viscous phase preferentially wets the solid walls, have been scarce and have yielded, somehow, puzzling results [7–9]. The first quantitative experiment in a prototypal Hele-Shaw geometry was performed with colloidal liquids only very recently [9]. Confocal imaging revealed a novel instability of the meniscus resulting in the formation of a liquid sheet in the midplane of the confinement. However, this instability does not interfere with the growth of the viscous fingers. In contrast, imbibition experiments in porous media had revealed a marked qualitative change in the morphologies of the invasion patterns [4,7,8].

Here, we revisit the seminal Saffman-Taylor experiment using water to displace viscous oils filling hydrophilic microfluidic channels. We demonstrate a novel type of liquid-entrainment instability and the subsequent growth of unanticipated imbibition patterns. We first quantitatively characterize their shape and propagation dynamics. We then theoretically elucidate that the intimate coupling between the short-scale molecular interactions with the solid and the large-scale flows results in the destabilization of the two-fluid interface. This model conveys a unified framework to consistently account for all the liquid entrainment scenarios that have been reported so far [9–11].

The experiment is thoroughly described in the Supplemental Material [12]. Briefly, a colored aqueous solution is injected into a microfluidic Hele-Shaw channel filled with silicon oil of viscosity η_{oil} ranging from 0.65 cp to to 3500 cp. The invasion patterns are observed with a CCD camera with a spacial resolution of 12 μm/pxl. To gain more knowledge about their 3D morphology, we also convert the transmitted-light intensity into the local water-pattern thickness with a resolution of 5 μm [13]. The channels are made by bonding two glass slides with double-sided tape. Prior to assembly, a thin film of thiolene-based resins is deposited on the two glass slides (NOA81, Norland Optical Adhesives). Using NOA81 surfaces, the advancing contact angle of the aqueous solution immersed in silicon oil can be continuously varied from $\theta_0 = 120 \pm 2°$ down to $\theta_0 = 7 \pm 2°$ by means of UV exposure [14]. The width and the length of the main channel are $W = 5$ mm, and $L = 4.5$ cm, respectively, Fig. 1. The channel height, $H = 100$ μm, is constant over the entire device and is unchanged as the fluids flow. The device is filled following a systematic sequence of injection steps described in Ref. [12]. This protocol prevents any possible modification of the wetting properties of the walls

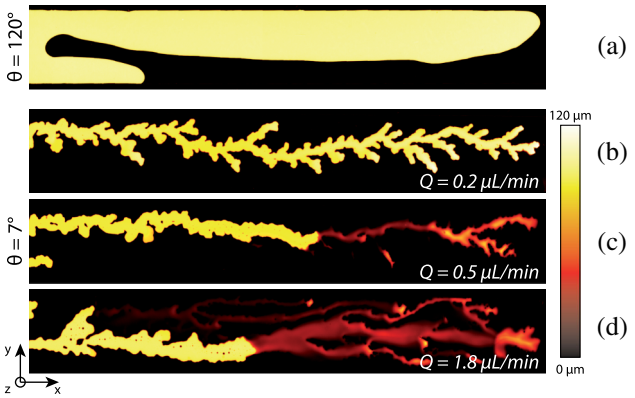

FIG. 1 (color online). Viscous fingering pattern, and associated water-thickness fields, $\eta_{\text{oil}} = 10^3$ cp. (a) Drainage pattern, $Q = 0.5\ \mu\text{l}/\text{min}$. (b), (c) and (d) Imbibition patterns observed at three different flow rates. See also movies 1, 2, and 3 in the Supplemental Material [12].

by the aqueous liquid prior to the imbibition experiment. In addition, the chips are *not* recycled. More than 50 chips were used to produced the data set introduced below.

We first show in Fig. 1(a) the result of a standard drainage experiment, where silicon oil of viscosity $\eta_{\text{oil}} = 10^3$ cp is displaced in an hydrophobic channel ($\theta_0 = 120°$). The wedge-shape entrance of the main channel (shown in a figure in the Supplemental Material [12]) promotes tip splitting in this typical Saffman-Taylor pattern [15]. The color coding in Fig. 1(a) indicates the local water thickness, the two fingers clearly fill the gap of the shallow channel. We also note that they grow along the side walls which they partly wet. The very same type of finger shapes were observed over a decade of flow rates: $0.2\ \mu\text{l}/\text{min} < Q < 1.8\ \mu\text{l}/\text{min}$. In contrast, Fig. 1(b) and movie 1 in the Supplemental Material [12] correspond to an imbibition experiment performed at small flow rate in an hydrophilic channel ($\theta_0 = 7°$). The marked difference between these two fingering patterns clearly reveals the impact of θ_0 on the water-front dynamics. The branching level is significantly increased while the width of the fingers is reduced compared to the drainage regime. More surprisingly, increasing the imposed water flow rate above $Q^\star = 0.4\ \mu\text{l}/\text{min}$, the imbibition dynamics does not reduce to the mere propagation of a sharp water front any more, see Figs. 1(c) and 1(d) and movies 2 and 3 in the Supplemental Material [12]. Thin water films are entrained from the finger tip throughout the oil phase, and merge to form complex interconnected patterns. Increasing the flow rate, the number of narrow thin films increases. Using a microscope and a 20× objective we found that the films propagate along the top and bottom walls. At this point we shall note that this latter observation is at odds with the entrainment dynamics reported in Ref. [9], where thin films were entrained in the midplane between the two confining walls.

Figure 2(a) conveys a clear picture of the interface dynamics at large scales. The imbibition-pattern thickness averaged over the y direction, $\langle h(x,y,t)\rangle_y$, is plotted as a function of time and of the x position along the channel. At $t = 0$, the flow rate is smaller than $Q^\star$, and a branched finger grows at a constant speed. As Q is increased above $Q^\star$, a thin water film is entrained and forms a rim. As sketched in Fig. 2(b), this rim is separated by the initial finger by an even thinner flat film. The rim moves at a constant speed ahead of the initial thick finger, which keeps on growing at a constant, yet smaller velocity. The local shape of the water-oil interface is sketched in Fig. 2(b). The main water finger slowly meanders in the channel following the interconnected track left by the entrained films thereby trapping small oil pockets in the channel. The topology of the resulting holey imbibition pattern, Fig. 1(d), is not akin to the branched structure emerging from a Laplacian growth process as observed in all the drainage experiments. This observation already suggests that the 3D nature of the fluid flows plays a significant role in this pattern formation [16].

In order to further characterize the pattern heterogeneities, we measured the instantaneous distribution $\mathcal{P}(h,t)$ of the film-thickness field. $\mathcal{P}(h,t)$ was found to be stationary, in agreement with the constant speed of the two fronts separating the three regions in Fig. 2(a) (finger, flat film, and rim). $\mathcal{P}(h)$ is typically composed of four peaks, that may overlap at high flow rates, Fig. 2(b). The leftmost peak corresponds to the edges of the pattern where the water thickness is by definition vanishingly small. The second peak corresponds to the flat-film regions. The third and broadest peak is centered on the typical rim-thickness value. The rightmost narrow peak located at $h = H$ corresponds to the main finger. The strong increase with Q of the leftmost-peak amplitude reflects the increase of the perimeter-over-surface ratio at high water injection rate. Figure 2(c) demonstrates that the mean thickness of the films $\langle h(x,y)\rangle_{x,y}$ decreases linearly with the imposed flow rate.

To gain more physical insight, we henceforth describe the imbibition process in terms of the three dimensionless numbers that control the interface dynamics: the advancing contact angle θ_0, the ratio of the ratio of the viscosity of the two fluids $\eta \equiv \eta_{\text{oil}}/\eta_{\text{water}}$, and the capillary number $\text{Ca} = \eta_{\text{water}} V/\gamma$, where V is the interface velocity, and γ is the surface energy of the two-fluids interface. We measured γ using the pendant drop method. γ does not depend on the silicon-oil molecular weight: $\gamma = 13 \pm 2$ mN/m. Here we focus on the roles of Ca and η for a small contact angle value, $\theta_0 = 7°$. Repeating the same experiment with oils of different viscosity, we measured the local and instantaneous velocity of the finger tip from which a water film is entrained. This measurement defines the critical capillary number $\text{Ca}^\star$ above which the meniscus is unstable. Unexpectedly, $\text{Ca}^\star$ undergoes nonmonotonic variations

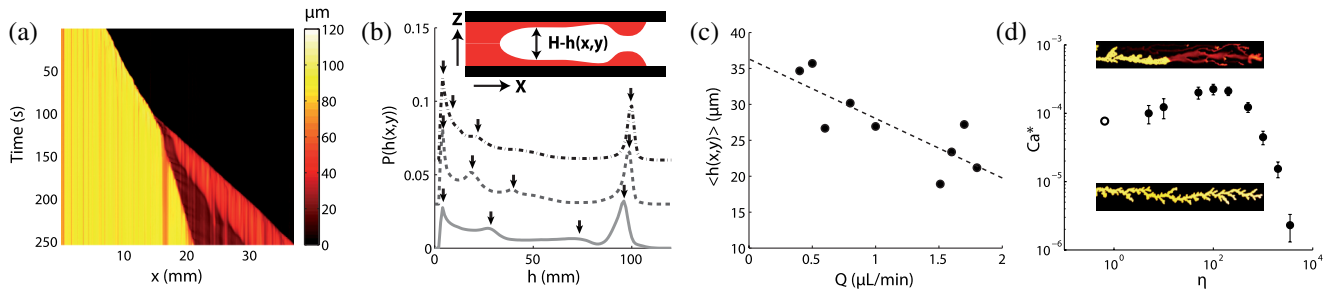

FIG. 2 (color online). Forced imbibition dynamics on a hydrophilic surface: $\theta_0 = 7°$. (a) Spatiotemporal plot of $\langle h(x,t)\rangle_y$ for $\eta_{\rm oil} = 10^3$ cp and Q = 1.5 μl/ min. (b) Sketch of the entrained film in the xz plane and probability distribution functions of the water-pattern thickness. Full line: Q = 1.8 μl/ min, dashed line: Q = 1.5 μl/ min, dotted line: Q = 0.5 μl/ min, $\eta_{\rm oil} = 10^3$ cp. The three curves are shifted by a constant offset to facilitate the reading. (c) Mean film thickness plotted versus the imposed water flow rate. (d) Phase diagram. Symbols: local critical capillary number at which entrainment occurs, $Ca^\star$ plotted versus the viscosity ratio between the two fluids, η. Error bars: one standard deviation.

with η and displays a maximum for $\eta \sim 100$, Fig. 2(d). This observation rules out a naive scaling argument which would consist in comparing the magnitudes of the Laplace pressure and of the viscous stress in the oil, or in the water phase at the macroscopic scale H. Such estimates would give a scaling law $\mathrm{Ca}^\star \sim 1/\eta$, or $\mathrm{Ca}^\star \sim 1$, none of which are experimentally observed. To go beyond this oversimplified description, we now introduce a minimal model which accounts for the interplay between the fluid flows and the meniscus shape at all scales.

For the sake of simplicity we ignore curvature effects in the xy plane, and focus on steadily moving interfaces that are translationally invariant along the y direction. In all that follows the interface is described in the frame moving with the contact line. The meniscus shape is determined by the *local* balance between the Laplace pressure and the normal-stress discontinuity across the fluid interface. Introducing the curvilinear coordinate along the interface, s, and the local interface curvature κ, the unit-vector normal to the surface $\hat{\mathbf{n}}$, this force-balance equation takes a compact form

$$\gamma\kappa(s)\hat{\mathbf{n}} = \Delta\boldsymbol{\sigma}\cdot\hat{\mathbf{n}}, \qquad (1)$$

where, the $\boldsymbol{\sigma}$ is the stress discontinuity at the interface. This equation couples to the Stokes equations for the two fluid flows. To solve this demanding problem, we built on Refs. [17,18], and make an additional ansatz which has proven to yield excellent agreement with lattice Boltzman simulations [19]. The velocity and the pressure fields in both phases are assumed to be locally given by the Hu and Scriven solutions for the flow in a wedge of angle $\theta(s)$, where $\theta(s)$ is the local angle between the tangent vector and the x axis, Fig. 3(a) [20]. Within this approximation, the stress discontinuity in Eq. (1) is readily computed, and the shape of the interface is fully prescribed by completing Eq. (1) with the boundary conditions: $\theta(s=0) = \theta_0$, $\theta(s=\ell/2) = \pi/2$, where ℓ is the curvilinear length of the meniscus. This boundary-value problem is then numerically solved first by recasting Eq. (1) into a four-dimensional dynamical system. The stress divergence at the contact line is regularized by introducing a finite slip length $\lambda \ll H$ at the walls. The resulting well-behaved differential equations are then integrated using an iterative collocation method as detailed in the Supplemental Material [12]. We shall note that the following results depend very weakly on λ which is henceforth set to $\lambda = 10^{-5}H$.

The evolution of the meniscus shape with the capillary number is shown in Fig. 3(a) for $\eta = 10^3$. Increasing Ca increases the meniscus length and reduces the apparent contact angle value $\theta_{\rm app}$. $\theta_{\rm app}$ is defined as the value of $\theta(s)$ where the interface curvature is minimal. More quantitatively, Fig. 3(b) shows that $\theta_{\rm app}$ decays to 0 for a finite value of Ca above which no stationary solution is found for the meniscus profile: in agreement with our experimental findings, a low-viscosity-liquid film is entrained along

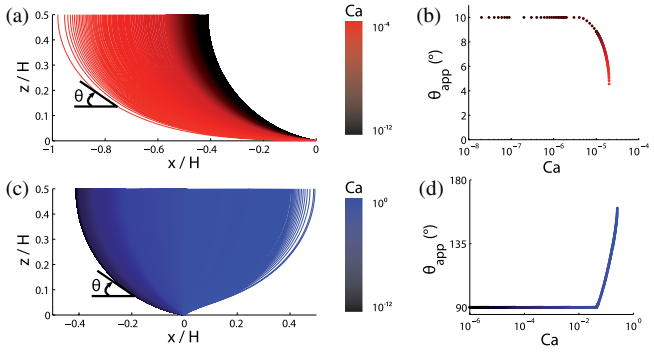

FIG. 3 (color online). (a) Computed meniscus profile for increasing values of Ca (from black to red). $\theta_0 = 10°$, $\eta = 10^3$, $\lambda/H = 10^{-5}$. (b) Variations of the apparent contact angle with Ca. Same parameters as in (a). (c) Computed meniscus profile for increasing values of Ca (from black to blue). $\theta_0 = 10°$, $\eta = 10^{-2}$, $\lambda/H = 10^{-5}$. (d) Variations of the apparent contact angle with Ca. Same parameters as in (c).

the walls. However, as exemplified in Fig. 3(c), when considering viscosity ratios smaller than $\eta^\star = 32$, we found another instability mechanism. As Ca increases, the apparent curvature of the meniscus decreases and changes sign. As a result, the apparent contact angle increases toward π, and above a critical Ca value, again, no stationary solution is found. However, this dual instability yields a meniscus shape opposite to the one found for $\eta > \eta^\star$; here a liquid sheet grows upstream in the midplane between the two walls. The interface profile shown in Fig. 3(c) corresponds to the one reported in Ref. [9] for colloidal liquids with moderate viscosity contrast, $\eta = 2.7$. Therefore our numerical results solve the apparent contradiction between Ref. [9] and our experimental findings: liquid menisci driven past solid surfaces can experience two qualitatively different liquid-entrainment instabilities. We stress that both scenarios echo the intricate coupling between the two fluid flows at the contact line. Even when it is associated with the smaller viscosity, the flow in the wetting phase significantly alters the stability of the meniscus upon imbibition dynamics. Sufficiently close to the contact line, due to the geometrical divergence of the strain rate, σ_{water} compares to σ_{oil}. In the absence of any intrinsic length scale in Eq. (1), and in the Stokes equation, the local modification of the meniscus curvature by the flow at the tip of the liquid wedge propagates up to the macroscopic scales.

To further check the consistency of our predictions, we conducted experiments with silicon oil having an ultralow viscosity, $\eta = 0.65$. Even though this viscosity ratio prevents the formation of viscous fingers in the xy plane, we did observe a strong change in the liquid motion at sufficiently high imposed flow rates. Again, above a critical (local) capillary number [open symbol in Fig. 2(d)], a liquid sheet is entrained between the two plates ahead of the main front, and subsequently rewets the confining wall. Incidentally, oil droplets are trapped on the two solid surfaces, see movie 4 in the Supplemental Material [12]. This observation is akin to the ones reported both in Ref. [9], and in Ref. [18] for air entrainment in a liquid bath. Together with our first experimental findings, this last experiment unambiguously confirms that, thin films can be entrained from a driven meniscus according to two different scenarios set by the magnitude of the viscosity ratio.

The two entrainment scenarios define the stability diagram computed numerically and plotted in Fig. 4(a). The stable meniscus region in the (η, Ca) plane is bounded by two critical curves $\mathrm{Ca}^\star = f(\eta)$, that meet at $\eta = \eta^\star$. Below $\eta^\star$ the entrained films propagate in the midplane of the gap, whereas above $\eta^\star$ entrainment occurs along the confining walls. This prediction captures well the salient features of the experimental phase diagram shown in Fig. 2(d). However, we did not achieve a quantitative agreement. For instance $\eta^\star$ was predicted to

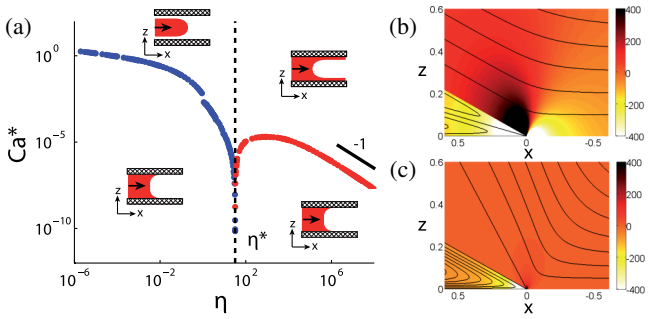

FIG. 4 (color online). Numerical results. (a) Stability diagram for a liquid interface driven in a Hele-Shaw channel: numerics. $\theta_0 = 10°$, $\lambda/H = 10^{-5}$. Insets: sketches of the interface shape in the xz plane. (b) Stream lines and pressure field in a wedge of angle $\theta_0 = 20°$ for $\eta/\eta^\star = 10$. Note the existence of a depression ahead of the contact line. (c) Stream lines and pressure field in a wedge of angle $\theta_0 = 20°$ for $\eta/\eta^\star = 0.1$. The color coding indicates the local pressure (arbitrary units).

be of the order of 32, yet it was measured to be close to unity. Needless to say that this discrepancy is not really surprising given the simplification of the meniscus geometry in the y direction, and potentially due to pinning effect at the contact line, which we have ignored.

Two last comments are in order. First, a simple criterion to distinguish between the two entrainment scenarios can be inferred from the flow-field geometry at the tip of the liquid wedge. In Figs. 4(b) and 4(c) we show the flows in a perfect wedge of angle θ_0 which is a reasonable approximation of the meniscus shape in the vicinity of the triple line. Below $\eta^\star$, Fig. 4(c), the stream lines in the low-viscosity liquid have a simple V shape. Conversely above $\eta^\star$, Fig. 4(b), they split into two recirculations. Simultaneously the radial velocity of the fluids at the interface changes sign. Hence, $\eta^\star$ is defined as the viscosity ratio at which the radial component of the interface velocity vanishes. Second, looking now at the pressure field in the oil phase, we can gain additional physical insight into the high $\eta > \eta^\star$ regime. Figure 4(b) indeed reveals that the tip of the liquid wedge is pulled downstream by a marked depression spot located at $z = 0$ in the oil phase, thereby promoting entrainment past the solid wall.

In summary, we have demonstrated a novel class of forced imbibition patterns. They stem from the entrainment of thin films out of the interface between a wetting fluid and a high viscosity fluid when driven past a solid surface. In addition, we have introduced a minimal theoretical framework which accounts well for all the imbibition-induced meniscus instabilities that have been reported so far. A challenging perspective to these results concerns the relevance and the impact of the meniscus instabilities to experiments closer to the actual oil-recovery processes, where the effect of wetting had been identified as a central control parameter [21].

We thank B. Andreotti, J. Snoeijer, and E. Santanach Carreras for illuminating discussions, and C. Odier for help with the experiments. D. B. acknowledges support from Institut Universitaire de France.

[1] Y. Couder, *Perspectives in Fluid Dynamics: A Collective Introduction to Current Research* (Cambridge University Press, Cambridge, England, 2002).
[2] D. Bensimon, L. Kananoff, S. Kiang, B. Shraiman, and C. Tang, Rev. Mod. Phys. **58**, 977 (1986).
[3] G. M. Homsy, Annu. Rev. Fluid Mech. **19**, 271 (1987).
[4] R. Lenormand, J. Phys. Condens. Matter **2**, SA79 (2001).
[5] P. G. Saffman and G. Taylor, Proc. R. Soc. A **245**, 312 (1958).
[6] M. Sahimi, Rev. Mod. Phys. **65**, 1393 (1993).
[7] D. A. Weitz, J. P. Stokes, R. O. Ball, and A. P. Kushnick, Phys. Rev. Lett. **59**, 2967 (1987).
[8] J. P. Stokes, D. A. Weitz, J. P. Gollub, A. Dougherty, M. O. Robbins, P. M. Chaikin, and H. M. Lindsay, Phys. Rev. Lett. **57**, 1718 (1986).
[9] S. A. Setu, I. Zacharoudiou, G. J. Davies, D. Bartolo, S. Moulinet, A. A. Louis, J. M. Yeomans, and D. G. A. L. Aarts, Soft Matter **9**, 10 599 (2013).
[10] J. H. Snoeijer and B. Andreotti, Annu. Rev. Fluid Mech., Vol. **45 45**, 269 (2013).
[11] R. Ledesma-Aguilar, A. Hernández-Machado, and I. Pagonabarraga, Phys. Rev. Lett. **110**, 264502 (2013).
[12] See Supplemental Material at http://link.aps.org/supplemental/10.1103/PhysRevLett.113.044501 for imbibition movies, a description of the experiments and of the simulation method, which includes Ref. [22].
[13] B. Saintyves, O. Dauchot, and E. Bouchaud, Phys. Rev. Lett. **111**, 047801 (2013).
[14] B. Levaché, A. Azioune, M. Bourrel, V. Studer, and D. Bartolo, Lab Chip **12**, 3028 (2012).
[15] E. Lajeunesse and Y. Couder, J. Fluid Mech. **419**, 125 (2000).
[16] M. B. Amar and D. Bonn, Physica D (Amsterdam) **209**, 1 (2005).
[17] J. H. Snoeijer, Phys. Fluids **18**, 021701 (2006).
[18] A. Marchand, T. S. Chan, J. H. Snoeijer, and B. Andreotti, Phys. Rev. Lett. **108**, 204501 (2012).
[19] T. S. Chan, S. Srivastava, A. Marchand, B. Andreotti, L. Biferale, F. Toschi, and J. H. Snoeijer, Phys. Fluids **25**, 074105 (2013).
[20] C. Huh and L. Scriven, J. Colloid Interface Sci. **35**, 85 (1971); D. M. Anderson and S. H. Davis, J. Fluid Mech. **257**, 1 (1993).
[21] N. Shahidzadeh, E. Bertrand, J.-P. Dauplait, J.-C. Borgotti, P. Vie, D. Bonn, Transp. Porous Media **52**, 213 (2003). N. Shahidzadeh-Bonn, A. Tournie, S. Bichon, P. Vie, S. Rodts, P. Faure, F. Bertrand, A. Azouni, Transp. Porous Media **56**, 209 (2004), and references therein.
[22] L. F. Shampine, I. Gladwell, and S. Thompson, *Solving ODEs with MATLAB* (Cambridge University Press, Cambridge, England, 2003).